Geophysical Research Letters

RESEARCH LETTER
10.1029/2025GL120872

Role of North Pacific Sea Surface Temperatures in Linking Summer Beaufort Sea Ice to Preceding-Winter ENSO

Shutao Cao[1], Anmin Duan[1], Xu Yuan[2], Yuzhuo Peng[1], and Ruizao Sun[3,4]

[1]Center for Marine Meteorology and Climate Change, State Key Laboratory of Marine Environmental Science, College of Ocean and Earth Sciences, Xiamen University, Xiamen, China, [2]Polar and Marine Research Institute, College of Harbor and Coastal Engineering, Jimei University, Xiamen, China, [3]China Meteorological Administration–Henan Key Laboratory of Agrometeorological Support and Applied Technique, Zhengzhou, China, [4]China Meteorological Administration–Henan Meteorological Service Center, Zhengzhou, China

Abstract Interannual variability of the Beaufort Sea (BFS) ice notably affects the oceanic circulation, pelagic and sympagic ecosystems, and navigation activities. However, key physical pathways regulating interseasonal connections between the El Niño-Southern Oscillation (ENSO) and BFS ice concentration anomalies in early-summer (May–July) remain unclear. Here, we established that winter (December-January-February) ENSO events, identified by the Niño 3 index, explained approximately 25% of BFS ice interannual variability in summer. We demonstrated that ENSO-induced North Pacific sea surface temperature (NPSST) anomalies persist into summer, triggering poleward-propagating Rossby waves by strengthening transient eddy vorticity forcing. The resulting anticyclonic and associated easterly anomalies over the BFS drive westward ice drift and subsequent ice reduction. ENSO-pacemaker simulations confirmed the causal relationship, estimating that NPSSTs contribute 61% to the ENSO-induced BFS ice anomalies in early summer. Our results emphasize the crucial role of NPSSTs for the ENSO-Arctic teleconnection, with important implications for seasonal sea-ice predictability.

Plain Language Summary The Beaufort Sea, a subregion of the Arctic ocean, exhibits large interannual changes in sea ice cover during summer. These can affect ocean circulation, marine ecosystems, and shipping activities. In this study, we established that the El Niño–southern oscillation (ENSO), a tropical climate pattern with global influence, accounted for approximately a quarter of sea ice variations in the Beaufort Sea in early summer. In particular, winter ENSO events caused an anomalous decrease in sea surface temperatures in the North Pacific that persisted into the following summer, altering winds over the Beaufort Sea, causing sea ice to drift westward, and reducing sea ice cover. Model simulations confirmed that winter ENSO events were the main drivers for these changes, with a contribution from North Pacific sea surface temperature anomalies exceeding 60%. These results demonstrate the strong connection between the ENSO and the Arctic Ocean; they will be useful to improve predictions of early-summer sea ice variations in the Beaufort Sea.

Key Points:

- Winter El Niño-Southern Oscillation events explain approximately 25% of sea-ice interannual variations in the Beaufort Sea in summer
- Associated North Pacific SSTs drive Beaufort Sea ice cover changes by modulating ice drift through an atmospheric bridge
- Fully-coupled climate model simulations reproduce the relationship between El Niño-Southern Oscillation events and Beaufort Sea ice cover

Supporting Information:

Supporting Information may be found in the online version of this article.

Correspondence to:

A. Duan,
amduan@xmu.edu.cn

Citation:

Cao, S., Duan, A., Yuan, X., Peng, Y., & Sun, R. (2026). Role of North Pacific sea surface temperatures in linking summer Beaufort sea ice to preceding-winter ENSO. *Geophysical Research Letters*, *53*, e2025GL120872. https://doi.org/10.1029/2025GL120872

Received 24 NOV 2025
Accepted 14 APR 2026

Author Contributions:

Conceptualization: Shutao Cao
Data curation: Shutao Cao
Formal analysis: Shutao Cao
Funding acquisition: Anmin Duan
Methodology: Shutao Cao
Project administration: Anmin Duan
Resources: Anmin Duan
Supervision: Anmin Duan
Validation: Shutao Cao
Visualization: Shutao Cao
Writing – original draft: Shutao Cao
Writing – review & editing: Anmin Duan, Xu Yuan, Yuzhuo Peng, Ruizao Sun

1. Introduction

Summer Arctic sea ice has undergone a rapid decline in recent decades (Ding et al., 2017; Stroeve & Notz, 2018), concurrently with pronounced interannual variability (Cai et al., 2021; Serreze & Stroeve, 2015). The Beaufort Sea (BFS) is among the Arctic subregions exhibiting the highest summer sea ice interannual variability (Figure S1a in Supporting Information S1), with a dominant period of approximately 4 years (Figures S1b and S1c in Supporting Information S1). Sea ice variations in the BFS critically regulate freshwater accumulation within the Beaufort Gyre (Armitage et al., 2020), which influences the oceanic circulation in the Arctic and globally (Q. Wang et al., 2025). Moreover, changes in BFS sea ice cover can markedly impact both its pelagic and sympagic ecosystems by altering their illumination conditions (Ardyna & Arrigo, 2020; Mundy et al., 2009). For human activities, seasonal reduction of the sea ice cover primarily determines the duration of the navigable season and the navigation capacity along the Northwest Passage (Mudryk et al., 2021). Therefore, understanding the drivers of sea-ice interannual variability is crucial.

Intrinsic local atmospheric variability is considered the dominant driver of summer Arctic sea ice variability, including the North Atlantic Oscillation (NAO; Cai et al., 2021; C. Wang et al., 2025), the Arctic Oscillation (AO; Ogi et al., 2016), the Arctic Dipole (Chang et al., 2022), and the Greenland anticyclone (Ding et al., 2017; Huang et al., 2021). During the negative phase of the NAO, circumpolar anticyclonic anomalies facilitate westward

transport of warm air from Greenland that can induce rapid sea-ice melt in the BFS (Liu et al., 2024). In addition, the regime shift in BFS ice toward younger, thinner ice since the 2000s has reduced its mechanical strength, thereby enhancing its mobility and dynamic response to atmospheric forcing (Babb et al., 2022). Similarly, several subsequent studies indicated that dynamically induced ice drift was an important contributor to interannual summer BFS sea-ice anomalies (Babb et al., 2022; Moore et al., 2022).

At a broader scale, the El Niño–Southern Oscillation (ENSO) can exert remote influences on Arctic sea ice through atmospheric bridges. Central Pacific El Niño events can suppress summer Arctic warming and sea-ice melt by strengthening circumpolar westerlies (Hu et al., 2016). Recent modeling studies (Baxter et al., 2019; Jeong et al., 2022) further attributed the accelerated decline of summer Arctic sea ice from the mid-2000s to 2012 to the frequent occurrences of La Niña events. However, it remains poorly explored whether ENSO, when reaching its peak intensity during winter, exerts a delayed influence on Arctic sea ice cover during the following summer, and through which physical pathways such a lagged response may occur. A recent study revealed a statistical relationship between the January Niño 3.4 index and subsequent summer sea ice in the BFS across multiple large-ensemble simulations, although this relationship is not significant in observations (Clancy et al., 2021). This relationship was attributed to ENSO-induced responses of the negative AO and deepened Aleutian Low (AL). However, the responses of AO and AL anomalies disappear during summer, with observational evidence indicating that significant responses are largely confined in winter, implying that the mechanisms linking winter ENSO to the BFS sea ice cover in the following summer remain largely uncertain.

Using observations, reanalysis data, and numerical simulations, here we investigate the statistical relationship between winter ENSO events and BFS sea ice concentration (BFS-SIC) in the following summer and characterize the possible physical mechanisms responsible for this delayed response. The article is organized as follows: data and methods used in this study are described in Section 2, the results are presented in Section 3 and discussed in Section 4, which also concludes the report.

2. Materials and Methods

2.1. Observational and Reanalysis Data

In this study, we used monthly Arctic sea ice concentration (SIC) of the Climate Data Record of Passive Microwave SIC, version 4 (Meier et al., 2021) retrieved from the National Snow and Ice Data Center (NSIDC). We also used monthly sea-ice motion (SIM) data from the Pan-Arctic Ice-Ocean Modeling and Assimilation System (PIOMAS; Zhang & Rothrock, 2003) to quantify the dynamic sea-ice drift. For monthly sea surface temperatures (SSTs), we used data with a spatial resolution of 1° from the Hadley Centre Sea Ice and Sea Surface Temperature data set (HadISST; Rayner et al., 2003). In addition, atmospheric fields were derived from the fifth-generation European Centre for Medium-Range Weather Forecast reanalysis (ERA5) data set (Hersbach et al., 2020).

The analysis period extended from 1979 to 2023, representing nearly 45 years during which satellite observations were available. All data sets were detrended to remove the influence of external forcings. Additionally, a 2–9 years bandpass filter was applied to preserve interannual signals. We defined seasonal means for winter, spring, and early summer as December-January-February (DJF), March-April-May (MAM), and May-June-July (MJJ), respectively, with the DJF period starting in December of the preceding year and occurring before MAM and MJJ.

2.2. Statistical Methods

We used conventional statistical methods including regression, correlation, and composite means analysis to diagnose observations and model simulations and a student's *t*-test to assess the statistical significance of our results. The significance level was 95% unless stated otherwise. We used wavelet power spectrum and wavelet coherence analysis to identify the dominant periodicities and examine the co-variability between time series. The Liang-Kleeman information flow method (Liang & Kleeman, 2005) was employed to infer the causality between variables independent of lead-lag relationship. We characterized the energy propagation of quasi-stationary Rossby waves by a horizontal wave activity flux W, expressed as in Equation 1 (Takaya & Nakamura, 2001):

$$W = \frac{p}{2|\boldsymbol{U}|}\begin{bmatrix} U\left(\varphi_x'^2 - \varphi'\varphi'_{xx}\right) + V\left(\varphi'_x\varphi'_y - \varphi'\varphi'_{xy}\right) \\ U\left(\varphi'_x\varphi'_y - \varphi'\varphi'_{xy}\right) + V\left(\varphi_y'^2 - \varphi'\varphi'_{yy}\right) \end{bmatrix} \quad (1)$$

where p indicates pressure, $U = (U, V)$ indicates the basic flow with its zonal and meridional components, $|U|$ indicates the horizontal wind speed, φ indicates the geostrophic stream function, and subscripts and prime symbols indicate spatial partial derivatives and time anomalies, respectively.

The root mean-square (RMS) of 2–8 day bandpass filtered daily 300-hPa geopotential height was used to reflect the activity of transient eddies (Blackmon, 1976). The Eady growth rate was used to characterize the baroclinicity of the atmosphere. And the impact of transient eddies on the seasonal-mean atmospheric circulation through vorticity forcing can be characterized by the geopotential tendency diagnosis (Cai et al., 2007):

$$\frac{\partial Z}{\partial t} = \frac{f}{g}\nabla^{-2}\left(-\nabla\left(\overrightarrow{V'}\,\xi'\right)\right) \quad (2)$$

Here, $\frac{\partial Z}{\partial t}$ represents the seasonal mean geopotential height tendency, g denotes the gravitational acceleration, f denotes the Coriolis parameter. $\vec{V}'$ and ξ' represent the synoptic-scale horizontal wind and relative vorticity, respectively.

2.3. Fully-Coupled Pacemaker Simulations

To investigate the possible physical mechanisms connecting winter ENSO events to Arctic sea ice during the following summer, we conducted SST-pacemaker simulations using the Community Earth System Model version 2 (CESM2; Danabasoglu et al., 2020). It is a fully-coupled climate model comprising atmosphere (CAM6), ocean (POP2), sea ice (CICE5), and other components. CAM6 is run on a finite-volume dynamical core with a horizontal resolution of 1.9° × 2.5°, while POP2 and CICE5 use the displaced pole grid with a 1° horizontal resolution. External forcings were set to their level in 2000.

We first conducted a 100-year control simulation to generate a model climatology and initial conditions for SST-pacemaker simulations. In the SST-pacemaker simulations, SSTs in the central-to-eastern tropical Pacific (180°W–90°W, 15°S–15°N) were nudged toward prescribed target fields constructed as observed monthly-varying El Niño composite SST anomalies superimposed on the model climatology (NG2Pos), and toward the model's monthly climatological SST (NG2Clim), while SSTs outside this region were allowed to evolve freely. Specifically, the El Niño composite anomalies were derived from years with DJF Niño 3 index exceeding 0.75 standard deviations. For both NG2Pos and NG2Clim, a time-slice run with 20 members, each integrated for 8 months, was initialized on 1 December of the last 20 years of the control simulation. SST nudging was applied throughout the model integration to accurately incorporate observed ENSO-related SST anomalies and their seasonal evolution. A buffer zone was created along the SST nudging region boundaries to ensure a smooth transition between the nudging and unconstrained areas (Figure S2 in Supporting Information S1). SST nudging was applied with a relaxation timescale of 5 days (Jeong et al., 2022). The ensemble-mean difference between NG2Pos and NG2Clim represented the model's response to El Niño-induced SST anomalies.

We conducted an additional set of simulations (NG2Pos_NPClim) to investigate the possible role of SSTs in the North Pacific (hereafter NPSST). In NG2Pos_NPClim, the model configuration was identical to that in NG2Pos, but with summer NPSSTs nudged to the long-term climatological mean to block possible ENSO-Arctic connections through the NPSST pathway. Thus, the ensemble-mean difference between NG2Pos_NPClim and NG2Clim represented the model's response to El Niño-induced SST anomalies without NPSST anomalies. The model configuration and relaxation masks are described in Table S1 and Figure S2 in Supporting Information S1.

2.4. ENSO Indices and Time Period Selection

In addition to conventional Niño indices including Niño 3, Niño 3.4, and Niño 4 (Trenberth, 1997), we also incorporated the warm pool and cold tongue Niño indices (WPNI and CTNI; Ren & Jin, 2011), the central and eastern Pacific Niño indices (CPNI and EPNI; Hu et al., 2016), along with the El Niño Modoki index (EMI; Ashok et al., 2007), to capture the full spectrum of linkages between ENSO and BFS-SIC variability. Niño 3,

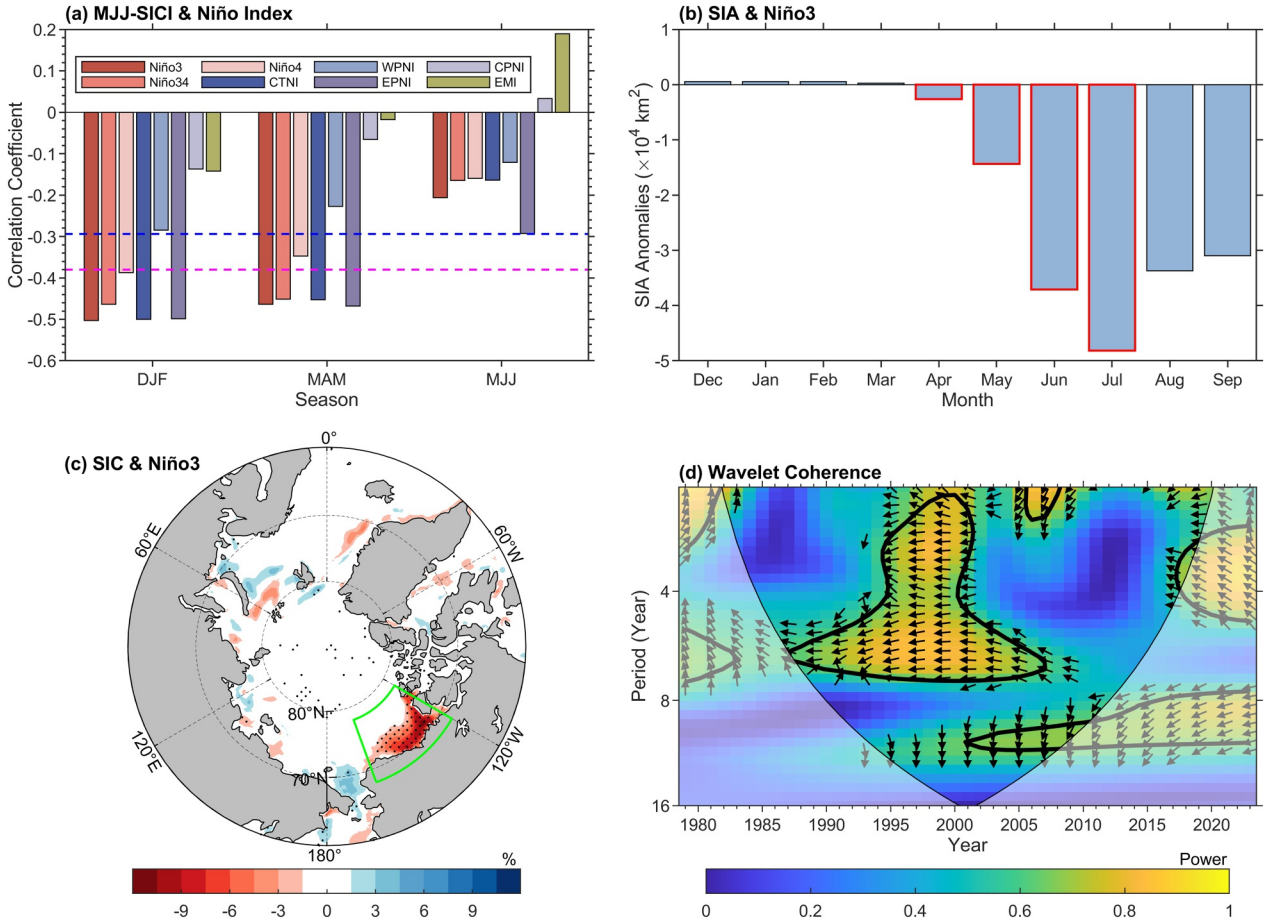

Figure 1. Connections between early summer (May-June-July, MJJ) Arctic sea ice and El Niño–southern oscillation (ENSO) conditions. (a) Correlations between the MJJ sea ice concentration index (SICI) over the Beaufort Sea (BFS) and seasonal Niño indices in December-January-February (DJF), March-April-May (MAM), and MJJ. (b) Regression of monthly BFS sea ice area (SIA) anomalies onto the normalized Niño 3 index in the preceding DJF. (c) Regression pattern of MJJ SIC in the BFS (green box; 160°W–120°W, 68°N–78°N) onto the normalized Niño 3 index in the preceding DJF. (d) Wavelet coherence analysis between the BFS-SICI and the Niño 3 index, with arrows representing the relative phase between the time series. Statistical significance: the 95% confidence level is indicated by the (a) blue dashed horizontal line (magenta: 99% confidence), (b) red edge, (c) stippling, and (d) thick black contour. The area enclosed by the thin curved line in (d) represents the cone of influence.

CTNI, and EPNI are consistently and highly correlated with the early-summer BFS sea ice concentration index (BFS-SICI; Figure 1a). Due to their exceptional consistency ($r > 0.95$), the choice of index does not qualitatively affect our conclusions; we therefore utilize Niño 3 as the primary proxy for the ENSO–BFS-SIC relationship. Similarly, we selected the MJJ period as summer months because it yielded the strongest correlations between the BFS-SICI and Niño indices for the preceding winter (Figure S3 in Supporting Information S1).

3. Results

3.1. Influence of Winter ENSO on BFS Ice Anomalies During the Following Summer

As justified in Section 2.4, here we used the DJF Niño 3 index to investigate the connection between winter ENSO events and Arctic sea ice in the following summer (MJJ), contrary to (Clancy et al., 2021) who adopted the Niño 3.4 index. The corresponding Pearson correlation coefficient was −0.50, suggesting that winter ENSO accounted for approximately 25% of the following-summer BFS-SIC variability. Conversely, the relationship between summer ENSO and BFS-SIC was weak and not statistically significant across ENSO diversity metrics (Figure 1a), suggesting that the direct influence of concurrent ENSO is negligible. The monthly response of the BFS sea ice area (hereafter BFS-SIA) to DJF-ENSO was strong in summer, but nearly negligible in winter and spring (Figure 1b). Moreover, when tropical Pacific SSTs indicated El Niño conditions in winter, pronounced,

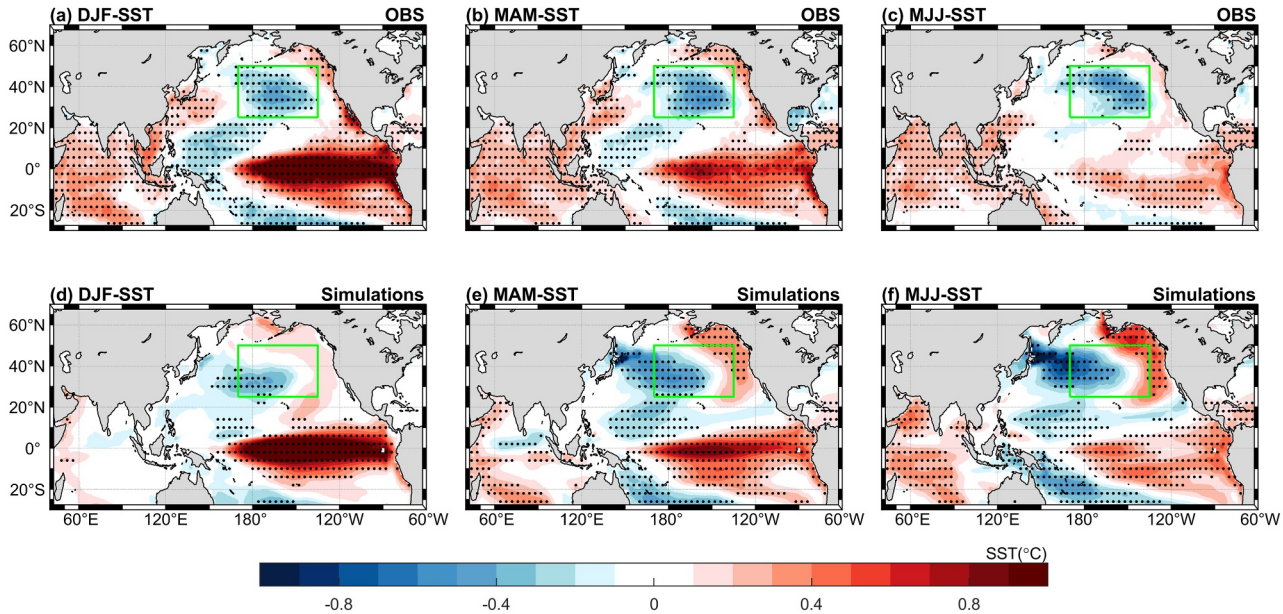

Figure 2. Observed (top) and simulated (bottom) seasonal sea surface temperature (SST) response over the tropical and North Pacific to preceding-winter ENSO. (a–c) Observed SST anomalies in DJF, MAM, and MJJ based on composite analysis using a ±0.75 standard deviation threshold of the DJF Niño 3 index. (d–f) Same as (a–c), but for the CESM2-simulated responses in the SST-pacemaker experiments (see text for details). Note that the SST anomaly amplitudes in (a–c) have been halved for comparability with the simulated response. The average SST value within the green box (170°E−135°W, 25°N–50°N) defines the North Pacific SST index (NPSSTI, see text). Stippling indicates statistical significance at the 95% confidence level.

spatially coherent negative SIC anomalies occurred nearly exclusively in the BFS during the following summer (Figure 1c). Wavelet coherence analysis (Figure 1d) further established strong and consistent interannual variations of the BFS-SICI and Niño 3 index, with representative timescales of 2–8 years.

3.2. NPSST Response to Winter ENSO

Previous studies (Clancy et al., 2021; Liu & Alexander, 2007) demonstrated that the ENSO can induce an AL-like response over the North Pacific through atmospheric teleconnections. However, short atmospheric memory would prevent winter ENSO-induced signals to persist until early summer. Therefore, characterizing the winter ENSO influence on the summer atmospheric circulation in the North Pacific and Arctic is crucial. Previous studies suggested that this influence could be exerted until the following summer through air-sea interactions, including the western North Pacific anticyclone (Wang et al., 2000), tropical Indian Ocean SST anomalies (Xie et al., 2009), and NPSST anomalies (Tao et al., 2024).

ENSO-related warm SST anomalies can create deep convection and upper-tropospheric divergence anomalies, generating a train of quasi-stationary Rossby waves that propagates northward from the tropical Pacific (Liu & Alexander, 2007). Downstream of the wave train, a Pacific-North American (PNA)-like pattern (Wallace & Gutzler, 1981) is observed, with negative geopotential height anomalies over the North Pacific (Figure S4a in Supporting Information S1). The wave train structure was barotropic, with enhanced AL response (Figure S4b in Supporting Information S1). Such cyclonic circulation anomalies strengthen climatological westerlies south of the AL (contours, Figure S4d in Supporting Information S1) and promote oceanic heat loss through turbulent heat fluxes (THF) at the air-sea interface (Figures S4c–S4e in Supporting Information S1). Accordingly, clear basin-scale cold NPSST anomalies during winter were present in the observations (Figure 2a) and reproduced in the SST-pacemaker simulations (Figure 2d), although the intensity was weaker than that of observations, which may arise from the absence of pre-winter tropical forcing in the pacemaker simulations. Moreover, the substantial ocean heat capacity allows winter NPSST anomalies to persist into the following summer (Sun et al., 2019), even as ENSO decays (Figures 2b, 2c, 2e, and 2f). The correlation between the MJJ NPSST index (NPSSTI, Figure 2) and preceding Niño 3 indices peaks in late winter and diminishes toward summer (Figure S5 in Supporting Information S1), indicating that summer NPSST anomalies are primarily a lagged response to the preceding winter ENSO. Empirical orthogonal function analysis reveals that ENSO-induced cold anomalies characterize the

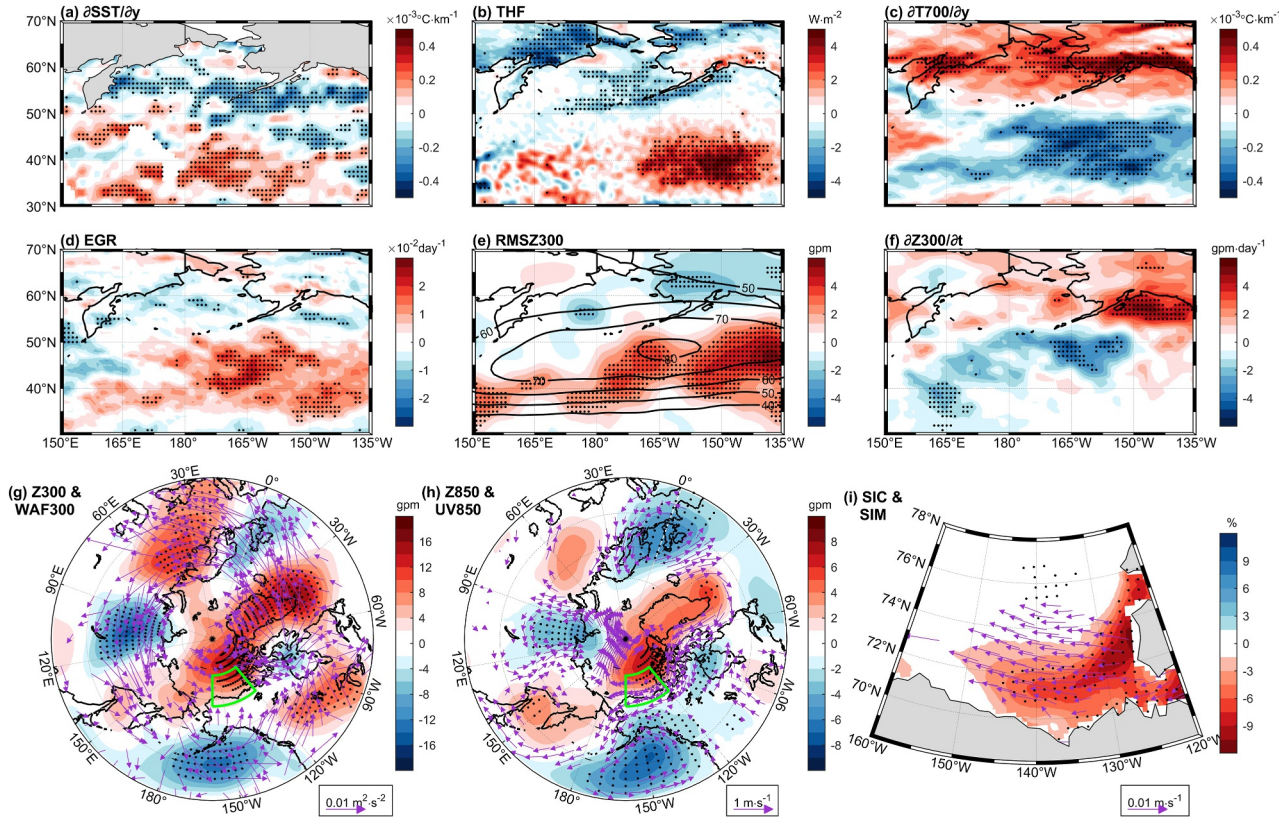

Figure 3. Physical processes through which NPSST influences atmospheric circulation and BFS-SIC anomalies in MJJ. (a) Regression pattern of the meridional SST gradient (∂SST/∂y) anomalies onto the NPSSTI. (b–i) Same as (a), but for (b) turbulent heat flux (THF); (c) 700-hPa meridional air temperature gradient (∂T700/∂y); (d) Eady growth rate (EGR); (e) root-mean-square of 300-hPa geopotential height (RMSZ300); (f) 300-hPa geopotential height tendency (∂Z300/∂t); (g) 300-hPa geopotential height (Z300, shadings) and wave activity flux (WAF300, vectors); (h) 850-hPa geopotential height (Z850, shadings) and horizontal wind (UV850, vectors); and (i) SIC and SIM anomalies, respectively. Black contours in (e) represent the climatological mean of RMSZ300. Stippling indicates statistical significance at the 95% confidence level; vectors below this level in (g–i) are not shown. The green boxes in (g) and (h) denote the BFS region. Note that all regression coefficients have been multiplied by −1 to represent patterns associated with cold NPSST anomalies.

second leading mode of summer NPSST (Figure S6b in Supporting Information S1), where the corresponding principal component and NPSSTI are strongly correlated ($r = 0.95$; Figure S6d in Supporting Information S1). The simulated cold SST extension into the Kuroshio–Oyashio Extension region (Figures 2e and 2f) represents a systematic bias (Zhang & Zhao, 2015) partly tied to the lack of Indian Ocean warming (Feng et al., 2021), as evident in our simulations (Figures 2d–2f). The Indian Ocean Basin Mode (IOBM) is a key ENSO-driven feature (Figure 2) that traditionally mediates North Pacific climate through Kelvin wave-induced anticyclones and the Pacific-Japan (PJ) pattern (Xie et al., 2009). Recent decoupling of the IOBM and PJ pattern (Xu et al., 2019), however, implies that the IOBM's impact on the North Pacific has substantially diminished.

3.3. NPSST Influences on Summer BFS-SIC

In this section, we investigate the mechanisms through which ENSO-induced persistent NPSST anomalies affect BFS sea ice. Observations and model simulations consistently indicated THF anomalies of opposite sign in winter and summer, suggesting a seasonal reversal of air-sea interactions (Figure S7 in Supporting Information S1). Causality diagnostics also reveal a dominant causal influence of SST on THF with negligible effects in the opposite direction (Figure S8 in Supporting Information S1), confirming the critical role of summer NPSST in modulating the regional atmospheric circulation.

Building on the framework that mid-to-high latitude SST anomalies can modulate geopotential height by affecting transient eddies (Fang & Yang, 2016), we diagnose the physical processes linking NPSST to Arctic atmospheric circulation and sea ice variability (Figure 3). The meridional SST gradient (Figure 3a) and THF anomalies (Figure 3b) associated with NPSST enhance atmospheric baroclinicity, evidenced by a steepened

meridional temperature gradient (Figure 3c) and increase in the Eady growth rate (Figure 3d). The strengthening of atmospheric baroclinicity facilitates active transient eddy activities in the upper troposphere (Figure 3e), further triggering negative geopotential tendency anomalies south of the Aleutian Islands as a dynamical response to eddy vorticity flux forcing (Figure 3f). With this disturbance, a Rossby wave train originating from North Pacific is excited, propagating across North America, Greenland, the Eurasian continent, and into the Arctic (Figure 3g), with the westerly jet stream potentially acting as a waveguide (Zhang et al., 2023). Characterized by a barotropic structure, the wave train generates an anomalous response resembling the Beaufort High over the western Arctic accompanied by low-level easterly wind anomalies along the BFS coast (Figure 3h), thereby driving westward sea ice drift and sea ice reduction (Figure 3i). Notably, the anticyclonic anomaly over the BFS and associated easterly anomalies remain evident in the pacemaker simulations (Figure S9 in Supporting Information S1), despite some differences in wave train structure. This indicates that the anticyclonic anomaly represents a robust atmospheric response to the preceding winter ENSO. Previous studies also suggest that sea ice can be influenced by variations in surface radiative fluxes associated with anticyclonic anomalies (Ding et al., 2017; Huang et al., 2021). However, the absence of robust surface radiative anomalies over the BFS in response to ENSO and NPSST (Figure S10 in Supporting Information S1) suggests that thermodynamic melting is not the primary mechanism of their associated early-summer BFS-SIC variability.

In the SST-pacemaker simulations, a response of notable negative SIC anomalies is evident in the eastern BFS region (Figure 4a), consistent with the observed pattern (Figure 3i). The monthly evolution of SIA anomalies further demonstrates that BFS ice cover remains largely insensitive to ENSO forcing until early summer (Figure 4c), consistent with observations (Figure 1b). The monthly sea ice tendency diagnostics (Figure S11 in Supporting Information S1) suggest that dynamical ice loss associated with sea ice drift is the primary driver of the summer BFS-SIC reduction. Quantitatively, our simulations suggest that El Niño events can induce a summer SIA anomaly of approximately 3.7×10^4 km^2 in the BFS (Figure 4c). Compared to observations, the simulated peak response occurs in June, 1 month earlier than observed (Figure 1b). This discrepancy likely arises from the model's overestimation of ENSO-induced dynamic ice export, leading to a premature depletion of marginal ice before the peak of the thermodynamic melting season (Figure S11 in Supporting Information S1). When the NPSST anomalies are excluded, the response of BFS-SIC to ENSO is substantially reduced, with the magnitude of the MJJ SIA response decreasing by 61% (Figure 4c), providing strong evidence for the crucial role of NPSST anomalies in linking the preceding winter ENSO to summer BFS-SIC variability.

4. Summary and Discussion

This study identified a robust teleconnection between winter ENSO and subsequent early-summer BFS sea ice, with NPSST acting as a critical interseasonal bridge. Specifically, winter ENSO triggers a positive PNA-like pattern through an atmospheric bridge, enhancing surface winds and upward turbulent heat fluxes and thereby inducing cold NPSST anomalies that persists into summer, representing the second leading mode of interannual SST variability in the North Pacific. In summer, cold NPSST anomalies enhance atmospheric baroclinicity and transient eddy activities, exciting a poleward-propagating Rossby wave train that manifests as a barotropic anticyclonic anomaly over the BFS. This atmospheric bridge, through associated coastal easterly anomalies, drives westward ice drift, ultimately leading to the observed sea ice reduction. SST-pacemaker simulations reproduce observed ENSO-induced BFS sea ice loss, confirming the robust teleconnection between winter ENSO and following-summer SIC. Conversely, excluding summer cold NPSST anomalies from the simulations reduced the magnitude of the summer BFS-SIC responses by approximately 61%, illustrating the critical role of NPSSTs in linking the tropical Pacific and the Arctic.

Our analysis focused on the relationship between ENSO and BFS-SIC at the interannual timescale; its stability in the current climate warming context and its sensitivity to the intrinsic decadal-scale variability of the climate system should be further investigated. The key role of NPSST anomalies in linking the ENSO and BFS-SIC suggests that the Pacific Decadal Oscillation (PDO) is likely a longer-period forcer of their interannual relationship. Previous studies demonstrated that the PDO can modulate the influence of the ENSO on global climate by altering background NPSSTs and ENSO-induced atmospheric teleconnections (Maher et al., 2022; Wang et al., 2008). The 21-year running correlation between ENSO and BFS-SIC suggests that their interannual relationship has undergone substantial temporal fluctuations in recent decades, despite remaining statistically significant during most periods (Figure S12 in Supporting Information S1). The ENSO-BFS SIC correlation is stronger during the positive phase of the PDO, likely because of colder background NPSSTs during positive PDO

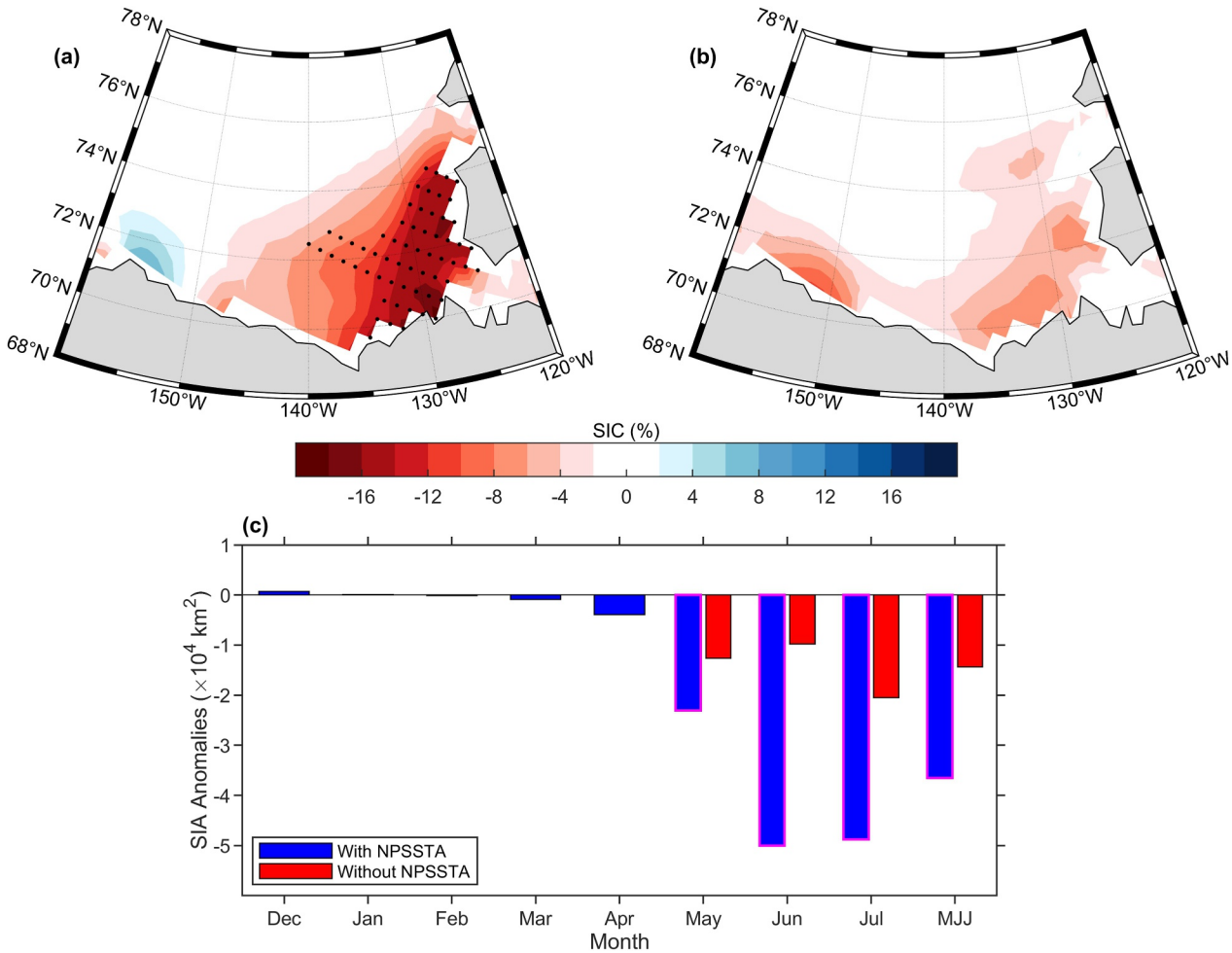

Figure 4. SIC and SIA anomalies over the BFS induced by DJF-ENSO in the SST-pacemaker simulations. (a) Response of MJJ SIC anomalies in the SST-pacemaker simulations (NG2Pos minus NG2Clim). (b) Same as (a), but for simulations without summer NPSST anomalies (NG2Pos_NPClim minus NG2Clim). (c) Monthly SIA anomalies (calculated on the native model grid) in December–July with (blue bars) and without (red bars) summer NPSST anomalies in response to DJF-ENSO. Stippling in (a, b) and magenta outline in (c) indicate statistical significance at the 95% confidence level.

phases. Moreover, the correlation exhibits a weakening trend, possibly associated with global warming. Further research is required to characterize the physical mechanisms linking winter ENSO and following summer BFS sea ice and to assess their temporal stability under future climate change projections.

Conflict of Interest

The authors declare no conflicts of interest relevant to this study.

Availability Statement

Data: All data sets used in this study are publicly available through open repositories. The monthly sea ice concentration data were obtained from the National Snow and Ice Data Center Climate Data Record of Passive Microwave Sea Ice Concentration, Version 4 (Meier et al., 2021). The monthly sea ice motion data were obtained from the Pan-Arctic Ice-Ocean Modeling and Assimilation System (Zhang & Rothrock, 2003). The ERA5 hourly data on pressure levels (Hersbach et al., 2023a), along with monthly averaged data on both single levels (Hersbach et al., 2023b) and pressure levels (Hersbach et al., 2023c), were obtained from the Copernicus Climate Change Service. The HadISST1.1 sea surface temperature data (Rayner et al., 2003) were obtained from the Met Office Hadley Centre. *Software*: Data processing and visualization were performed using MATLAB (version R2023b)

and NCAR Command Language (version 6.6.2). The primary diagnostic and plotting scripts can be accessed through the Zenodo repository (Cao, 2026). The CESM2 (Danabasoglu et al., 2020) source code used for the pacemaker simulations was provided by the National Center for Atmospheric Research.

Acknowledgments
This work was supported by the National Natural Science Foundation of China under Grants U2442205 and 42030602. Y.P. was also supported by the China Scholarship Council (Grant 202306310197) and the China Postdoctoral Science Foundation (Grant 2023M742910). We thank Eric Dupuy, Ph.D., from Liwen Bianji (Edanz) (www.liwenbianji.cn), for editing the English text of a draft of this manuscript.

References

Ardyna, M., & Arrigo, K. R. (2020). Phytoplankton dynamics in a changing Arctic Ocean. *Nature Climate Change*, *10*(10), 892–903. https://doi.org/10.1038/s41558-020-0905-y

Armitage, T. W., Manucharyan, G. E., Petty, A. A., Kwok, R., & Thompson, A. F. (2020). Enhanced eddy activity in the beaufort gyre in response to sea ice loss. *Nature Communications*, *11*(1), 761. https://doi.org/10.1038/s41467-020-14449-z

Ashok, K., Behera, S. K., Rao, S. A., Weng, H., & Yamagata, T. (2007). El Niño Modoki and its possible teleconnection. *Journal of Geophysical Research*, *112*(C11), C11007. https://doi.org/10.1029/2006JC003798

Babb, D. G., Galley, R. J., Howell, S. E., Landy, J. C., Stroeve, J. C., & Barber, D. G. (2022). Increasing multiyear sea ice loss in the Beaufort Sea: A new export pathway for the diminishing multiyear ice cover of the Arctic Ocean. *Geophysical Research Letters*, *49*(9), e2021GL097595. https://doi.org/10.1029/2021GL097595

Baxter, I., Ding, Q., Schweiger, A., L'Heureux, M., Baxter, S., Wang, T., et al. (2019). How tropical Pacific surface cooling contributed to accelerated sea ice melt from 2007 to 2012 as ice is thinned by anthropogenic forcing. *Journal of Climate*, *32*(24), 8583–8602. https://doi.org/10.1175/JCLI-D-18-0783.1

Blackmon, M. L. (1976). A climatological spectral study of the 500 mb geopotential height of the Northern Hemisphere. *Journal of the Atmospheric Sciences*, *33*(8), 1607–1623. https://doi.org/10.1175/1520-0469(1976)033<1607:ACSSOT>2.0.CO;2

Cai, M., Yang, S., Van Den Dool, H., & Kousky, V. (2007). Dynamical implications of the orientation of atmospheric eddies: A local energetics perspective. *Tellus A: Dynamic Meteorology and Oceanography*, *59*(1), 127–140. https://doi.org/10.1111/j.1600-0870.2006.00213.x

Cai, Q., Beletsky, D., Wang, J., & Lei, R. (2021). Interannual and decadal variability of Arctic summer sea ice associated with atmospheric teleconnection patterns during 1850–2017. *Journal of Climate*, *34*(24), 9931–9955. https://doi.org/10.1175/JCLI-D-20-0330.1

Cao, S. (2026). Data and codes used in the study role of North Pacific Sea surface temperatures in linking summer beaufort Sea ice to preceding-winter ENSO [Software]. *Zenodo*. https://doi.org/10.5281/zenodo.19060550

Chang, L., Morioka, Y., Behera, S., Luo, J. J., Xu, H., & Zhou, B. (2022). What mainly drives the interannual climate variability over the barents-kara seas in boreal early autumn? *Journal of Geophysical Research: Atmospheres*, *127*(21), e2021JD036216. https://doi.org/10.1029/2021JD036216

Clancy, R., Bitz, C., & Blanchard-Wrigglesworth, E. (2021). The influence of ENSO on Arctic sea ice in large ensembles and observations. *Journal of Climate*, *34*(24), 9585–9604. https://doi.org/10.1175/JCLI-D-20-0958.1

Danabasoglu, G., Lamarque, J. F., Bacmeister, J., Bailey, D., DuVivier, A., Edwards, J., et al. (2020). The community earth system model version 2 (CESM2). *Journal of Advances in Modeling Earth Systems*, *12*(2), e2019MS001916. https://doi.org/10.1029/2019ms001916

Ding, Q., Schweiger, A., L'Heureux, M., Battisti, D. S., Po-Chedley, S., Johnson, N. C., et al. (2017). Influence of high-latitude atmospheric circulation changes on summertime Arctic sea ice. *Nature Climate Change*, *7*(4), 289–295. https://doi.org/10.1038/nclimate3241

Fang, J., & Yang, X.-Q. (2016). Structure and dynamics of decadal anomalies in the wintertime midlatitude North Pacific ocean–atmosphere system. *Climate Dynamics*, *47*(5), 1989–2007. https://doi.org/10.1007/s00382-015-2946-x

Feng, J., Lian, T., Chen, D., & Li, Y. (2021). The cause of the large cold bias in the northwestern Pacific Ocean. *Geophysical Research Letters*, *48*(18), e2021GL094616. https://doi.org/10.1029/2021GL094616

Hersbach, H., Bell, B., Berrisford, P., Biavati, G., Horányi, A., Muñoz Sabater, J., et al. (2023a). ERA5 hourly data on pressure levels from 1940 to present [Dataset]. *Copernicus Climate Change Service (C3S) Climate Data Store (CDS)*. https://doi.org/10.24381/cds.bd0915c6

Hersbach, H., Bell, B., Berrisford, P., Biavati, G., Horányi, A., Muñoz Sabater, J., et al. (2023b). ERA5 monthly averaged data on single levels from 1940 to present [Dataset]. *Copernicus Climate Change Service (C3S) Climate Data Store (CDS)*. https://doi.org/10.24381/cds.f17050d7

Hersbach, H., Bell, B., Berrisford, P., Biavati, G., Horányi, A., Muñoz Sabater, J., et al. (2023c). ERA5 monthly averaged data on pressure levels from 1940 to present [Dataset]. *Copernicus Climate Change Service (C3S) Climate Data Store (CDS)*. https://doi.org/10.24381/cds.6860a573

Hersbach, H., Bell, B., Berrisford, P., Hirahara, S., Horányi, A., Muñoz-Sabater, J., et al. (2020). The ERA5 global reanalysis. *Quarterly journal of the royal meteorological society*, *146*(730), 1999–2049. https://doi.org/10.1002/qj.3803

Hu, C., Yang, S., Wu, Q., Li, Z., Chen, J., Deng, K., et al. (2016). Shifting El Niño inhibits summer Arctic warming and Arctic sea-ice melting over the Canada Basin. *Nature Communications*, *7*(1), 11721. https://doi.org/10.1038/ncomms11721

Huang, Y., Ding, Q., Dong, X., Xi, B., & Baxter, I. (2021). Summertime low clouds mediate the impact of the large-scale circulation on Arctic sea ice. *Communications Earth & Environment*, *2*(1), 38. https://doi.org/10.1038/s43247-021-00114-w

Jeong, H., Park, H. S., Stuecker, M. F., & Yeh, S. W. (2022). Record low Arctic sea ice extent in 2012 linked to two-year La Niña-driven sea surface temperature pattern. *Geophysical Research Letters*, *49*(9), e2022GL098385. https://doi.org/10.1029/2022GL098385

Liang, X. S., & Kleeman, R. (2005). Information transfer between dynamical system components. *Physical Review Letters*, *95*(24), 244101. https://doi.org/10.1103/PhysRevLett.95.244101

Liu, L., Zhang, W., Liu, C., & Jiang, F. (2024). Important influence of North Atlantic oscillation on interannual variability of the boreal autumn east siberian–beaufort sea ice. *Journal of Climate*, *37*(2), 639–653. https://doi.org/10.1175/JCLI-D-23-0341.1

Liu, Z., & Alexander, M. (2007). Atmospheric bridge, oceanic tunnel, and global climatic teleconnections. *Reviews of Geophysics*, *45*(2), RG2005. https://doi.org/10.1029/2005RG000172

Maher, N., Kay, J. E., & Capotondi, A. (2022). Modulation of ENSO teleconnections over North America by the Pacific decadal oscillation. *Environmental Research Letters*, *17*(11), 114005. https://doi.org/10.1088/1748-9326/ac9327

Meier, W. N., Fetterer, F., Windnagel, A. K., & Stewart, J. S. (2021). NOAA/NSIDC climate data record of passive microwave sea Ice concentration, version 4 [Dataset]. *NSIDC: National Snow and Ice Data Center*. https://doi.org/10.7265/efmz-2t65

Moore, G., Steele, M., Schweiger, A. J., Zhang, J., & Laidre, K. L. (2022). Thick and old sea ice in the Beaufort Sea during summer 2020/21 was associated with enhanced transport. *Communications Earth & Environment*, *3*(1), 198. https://doi.org/10.1038/s43247-022-00530-6

Mudryk, L. R., Dawson, J., Howell, S. E., Derksen, C., Zagon, T. A., & Brady, M. (2021). Impact of 1, 2 and 4 C of global warming on ship navigation in the Canadian Arctic. *Nature Climate Change*, *11*(8), 673–679. https://doi.org/10.1038/s41558-021-01087-6

Mundy, C., Gosselin, M., Ehn, J., Gratton, Y., Rossnagel, A., Barber, D. G., et al. (2009). Contribution of under-ice primary production to an ice-edge upwelling phytoplankton bloom in the Canadian Beaufort Sea. *Geophysical Research Letters*, *36*(17). https://doi.org/10.1029/2009GL038837

Ogi, M., Rysgaard, S., & Barber, D. G. (2016). Importance of combined winter and summer Arctic Oscillation (AO) on September sea ice extent. *Environmental Research Letters*, *11*(3), 034019. https://doi.org/10.1088/1748-9326/11/3/034019

Rayner, N. A., Parker, D. E., Horton, E., Folland, C. K., Alexander, L. V., Rowell, D., et al. (2003). Global analyses of sea surface temperature, sea ice, and night marine air temperature since the late nineteenth century. *Journal of Geophysical Research*, *108*(D14), 4407. https://doi.org/10.1029/2002JD002670

Ren, H. L., & Jin, F. F. (2011). Niño indices for two types of ENSO. *Geophysical Research Letters*, *38*(4), L04704. https://doi.org/10.1029/2010GL046031

Serreze, M. C., & Stroeve, J. (2015). Arctic sea ice trends, variability and implications for seasonal ice forecasting. *Philosophical Transactions of the Royal Society A: Mathematical, Physical & Engineering Sciences*, *373*(2045), 20140159. https://doi.org/10.1098/rsta.2014.0159

Stroeve, J., & Notz, D. (2018). Changing state of Arctic sea ice across all seasons. *Environmental Research Letters*, *13*(10), 103001. https://doi.org/10.1088/1748-9326/aade56

Sun, R., Duan, A., Chen, L., Li, Y., Xie, Z., & Zhao, Y. (2019). Interannual variability of the North Pacific mixed layer associated with the spring Tibetan Plateau thermal forcing. *Journal of Climate*, *32*(11), 3109–3130. https://doi.org/10.1175/jcli-d-18-0577.1

Takaya, K., & Nakamura, H. (2001). A formulation of a phase-independent wave-activity flux for stationary and migratory quasigeostrophic eddies on a zonally varying basic flow. *Journal of the Atmospheric Sciences*, *58*(6), 608–627. https://doi.org/10.1175/1520-0469(2001)058<0608:AFOAPI>2.0.CO;2

Tao, L., Yang, X. Q., Sun, L., Sun, X., Fang, J., Cai, D., et al. (2024). Meridional path of ENSO impact on following early-summer North Pacific climate. *Geophysical Research Letters*, *51*(18), e2024GL111079. https://doi.org/10.1029/2024GL111079

Trenberth, K. E. (1997). The definition of el nino. *Bulletin of the American Meteorological Society*, *78*(12), 2771–2778. https://doi.org/10.1175/1520-0477(1997)078<2771:tdoeno>2.0.co;2

Wallace, J. M., & Gutzler, D. S. (1981). Teleconnections in the geopotential height field during the Northern Hemisphere winter. *Monthly Weather Review*, *109*(4), 784–812. https://doi.org/10.1175/1520-0493(1981)109<0784:titghf>2.0.co;2

Wang, B., Wu, R., & Fu, X. (2000). Pacific–East Asian teleconnection: How does ENSO affect East Asian climate? *Journal of Climate*, *13*(9), 1517–1536. https://doi.org/10.1175/1520-0442(2000)013<1517:PEATHD>2.0.CO;2

Wang, C., Su, H., Zhai, C., Zheng, J., Yu, S., Mo, H., et al. (2025). Recent slowing of Arctic sea ice melt tied to multidecadal NAO variability. *Nature Communications*, *16*(1), 8504. https://doi.org/10.1038/s41467-025-63520-0

Wang, L., Chen, W., & Huang, R. (2008). Interdecadal modulation of PDO on the impact of ENSO on the East Asian winter monsoon. *Geophysical Research Letters*, *35*(20), L20702. https://doi.org/10.1029/2008GL035287

Wang, Q., Shu, Q., Wang, S., Li, X., Danilov, S., Qiao, F., et al. (2025). Dominant inflation of the Arctic Ocean's Beaufort Gyre in a warming climate. *Communications Earth & Environment*, *6*(1), 40. https://doi.org/10.1038/s43247-025-02028-3

Xie, S.-P., Hu, K., Hafner, J., Tokinaga, H., Du, Y., Huang, G., & Sampe, T. (2009). Indian Ocean capacitor effect on indo–western Pacific climate during the summer following El Niño. *Journal of Climate*, *22*(3), 730–747. https://doi.org/10.1175/2008JCLI2544.1

Xu, P., Wang, L., Chen, W., Feng, J., & Liu, Y. (2019). Structural changes in the Pacific–Japan pattern in the late 1990s. *Journal of Climate*, *32*(2), 607–621. https://doi.org/10.1175/JCLI-D-18-0123.1

Zhang, C., Duan, A., Jia, X., Wang, Z., & Pan, Z. (2023). A dynamic link between spring Arctic sea ice and the Tibetan Plateau snow increment indicator. *npj Climate and Atmospheric Science*, *6*(1), 191. https://doi.org/10.1175/JCLI-D-18-0123.1

Zhang, J., & Rothrock, D. A. (2003). Modeling global sea ice with a thickness and enthalpy distribution model in generalized curvilinear coordinates. *Monthly Weather Review*, *131*(5), 845–861. https://doi.org/10.1175/1520-0493(2003)131<0845:MGSIWA>2.0.CO;2

Zhang, L., & Zhao, C. (2015). Processes and mechanisms for the model sst biases in the north atlantic and north pacific: A link with the a tlantic meridional overturning circulation. *Journal of Advances in Modeling Earth Systems*, *7*(2), 739–758. https://doi.org/10.1002/2014MS000415